Journal of Materials Chemistry A

# Rational Synthesis and Electrochemical Performance of $LiVOPO_4$ Polymorphs

| | |
|---|---|
| Journal: | *Journal of Materials Chemistry A* |
| Manuscript ID | TA-ART-12-2018-012531.R1 |
| Article Type: | Paper |
| Date Submitted by the Author: | 28-Feb-2019 |
| Complete List of Authors: | Hidalgo, Marc F.; Binghamton University, Materials Science and Engineering<br>Lin, Yuh-Chieh; University of California San Diego, Department of NanoEngineering<br>Grenier, Antonin; Argonne National Laboratory, X-ray Science Division, Advanced Photon Source<br>Xiao, Dongdong; Binghamton University<br>Rana, Jatinkumar; Binghamton University, Applied Physics and Astronomy<br>Xin, Huolin; Brookhaven National Laboratory, Center for Functional Nanomaterials<br>Tran, Richard; University of California San Diego, Department of NanoEngineering<br>Zuba, Mateusz; Binghamton University, Physics, Applied Physics and Astronomy<br>Donohue, Jennifer; Binghamton University<br>Omenya, Frederick; Binghamton University<br>Chu, Iek-Heng; University of California San Diego, Department of NanoEngineering<br>Wang, Zhenbin; University of California San Diego, Department of NanoEngineering<br>Li, XiangGuo; University of California San Diego, Department of NanoEngineering<br>Chernova, Natasha; Binghamton University<br>Chapman, Karena; Argonne National Laboratory<br>Zhou, Guangwen; Binghamton University, Mechanical Engineering<br>Piper, Louis; Binghamton University, Department of Physics, Applied Physics, and Astronomy<br>Ong, Shyue Ping; University of California San Diego, Department of NanoEngineering<br>Whittingham, M.; Binghamton University, Department of Chemistry |
| | |

Journal Name

ARTICLE

# Rational Synthesis and Electrochemical Performance of $LiVOPO_4$ Polymorphs

Received 00th January 20xx,
Accepted 00th January 20xx

DOI: 10.1039/x0xx00000x

**www.rsc.org/**

Marc Francis V. Hidalgo,[a$] Yuh-Chieh Lin,[b$] Antonin Grenier,[c] Dongdong Xiao,[d] Jatinkumar Rana,[a] Richard Tran,[b] Huolin Xin,[d] Mateusz Zuba,[a] Jennifer Donohue,[a] Fredrick O. Omenya,[a] Iek-Heng Chu,[b] Zhenbin Wang,[b] XiangGuo Li,[b] Natasha A. Chernova,[a] Karena W. Chapman,[c] Guangwen Zhou,[d] Louis Piper,[a] Shyue Ping Ong,*[b] and M. Stanley Whittingham*[a]

$LiVOPO_4$ is a promising cathode material for Li-ion batteries due to its ability to intercalate up to two electrons per vanadium redox center. However, $LiVOPO_4$ exhibits polymorphism, forming either the $\alpha_I$, β, or ε phase. A thorough comparison between the properties of these phases is difficult because they usually differ in synthesis methods. In this study, we synthesize all three polymorphs by annealing a single precursor, $LiVOPO_4{\cdot}2H_2O$, thereby reducing the effect of synthesis on the properties of the materials. We show through in-situ XRD with heating and DFT calculations that, in terms of stability, $\alpha_I$-$LiVOPO_4$ <<< ε-$LiVOPO_4$ ≤ β-$LiVOPO_4$. We also show experimentally and through DFT calculations that the tolerance to O-interstitials and O-vacancies can explain the differences in stability, morphology, and electrochemical performance between β- and ε-$LiVOPO_4$. β-$LiVOPO_4$ is more stable in the presence of O-interstitials while ε-$LiVOPO_4$ is favored in the presence of O-vacancies. These defects affect the surface energies and morphology of the products formed, which are confirmed in the Wulff shape calculations and Transmission Electron Microscopy images. These imply that β-$LiVOPO_4$ has an improved rate performance under an oxidizing atmosphere due to the increased presence of facets with superior ion diffusion at the surface. This improved performance is seen by the improved rate capability and capacity of β-$LiVOPO_4$ in the high-voltage region. In contrast, synthesis conditions have little effect on improving the rate performance of ε-$LiVOPO_4$.

## Introduction

Li-ion batteries utilizing intercalation chemistry are currently the most prominent form of energy storage for portable electronic devices and electric vehicles due to their high energy density.[1-6] Unfortunately, the capacity of most commercially available cathode materials is limited by the fact that the cathode material can only store up to one $Li^+$ ion per redox center. Thus, there is a large interest in materials which can intercalate multiple electrons per redox center.[7-14] One such material is lithium vanadyl phosphate, or $LiVOPO_4$.[15-17] The $V^{5+}/V^{4+}$ and $V^{4+}/V^{3+}$ redox couples at 4.0 V and 2.5 V, respectively, allow for the intercalation of up to two $Li^+$ ions per vanadium through the formation of $VOPO_4 \leftrightarrow LiVOPO_4 \leftrightarrow Li_2VOPO_4$ during the operation of the battery. This results in a high theoretical capacity of 305 mAh/g and a specific energy of over 900 Wh/g.[18-20]

Three major polymorphs of $LiVOPO_4$, $\alpha_I$-, β-, and ε-$LiVOPO_4$, have been previously reported and synthesized through different methods. The $\alpha_I$ phase (tetragonal, P4/nmm)[21-24] has a layered structure exhibiting 2D Li diffusion, and is the least reported among the different polymorphs due to difficulties in its synthesis. On the other hand, the β phase (orthorhombic, Pnma)[25-27] has 1D diffusion channels while the ε phase (triclinic, $P\overline{1}$)[17, 25, 28-30] has pseudo-1D diffusion channels. Unlike $\alpha_I$, both the β and ε phases have been synthesized using a large plethora of methods, including hydrothermal,[17, 20, 31] solid-state,[28, 31-33] and sol-gel.[32, 34]

A complete understanding of the differences between these phases is essential to identifying which polymorph is best suited as a cathode material in a Li-ion battery. Thermodynamic calculations have reported previously that $\alpha_I$ is metastable relative to both β and ε, which have very similar stabilities.[16, 29] Additionally, the different phases have been observed and reported either transforming between one another or appearing as impurities.[25, 34-36] However, since the difference in stability of these phases is small, minute differences in synthesis would greatly influence the individual properties of the

---

[$] *Equal contribution*
[a] *NECCES, Binghamton University, Binghamton, NY 13902, USA. Email: stanwhit@gmail.com*
[b] *Department of NanoEngineering, University of California San Diego, 9500 Gilman Drive #0448, La Jolla, CA 92093, USA. *Email: ongsp@eng.ucsd.edu*
[c] *X-ray Science Division, Advanced Photon Source, Argonne National Laboratory, 9700 South Cass Avenue, Lemont, IL 60439, USA*
[d] *Center for Functional Nanomaterials, Brookhaven National Laboratory, Upton, NY, 11973, USA*

Electronic Supplementary Information (ESI) available: [details of any supplementary information available should be included here]. See DOI: 10.1039/x0xx00000x

polymorphs. This makes it difficult to conduct a thorough comparison of different properties of the polymorphs.

To address this challenge, we show in this study that all three polymorphs can be synthesized from a single precursor, $LiVOPO_4{\cdot}2H_2O$, through careful control of synthesis conditions. By utilizing a single precursor, it is possible to minimize effects of synthesis on the properties such as stability and electrochemical performance, allowing for more direct and accurate experimental and theoretical comparisons. In addition, we demonstrated that the limitations to the electrochemical performance of $LiVOPO_4$ due to electronic and ionic conductions can be remedied with carbon coating, nano-sizing, and morphology control.[16, 17] Guided by DFT surface calculations, we demonstrate how control of the O chemical potential may be used to control morphology to promote the formation of facets with facile Li intercalation[37-39] for high rate performance.

## Methodology

### Experimental Methods

**Synthesis of $LiVOPO_4{\cdot}2H_2O$ and different $LiVOPO_4$ polymorphs.**

The $LiVOPO_4{\cdot}2H_2O$ precursor was synthesized using a hydrothermal method modified from previous reports.[30] $V_2O_5$ (Aldrich, >99.6%), oxalic acid (Sigma-Aldrich, >99.0%), and phosphoric acid (Fisher Scientific, 85%) were dissolved in ethanol and water, and stirred for 18 hours. $LiOH{\cdot}H_2O$ (Sigma, >99.0%) was then added, and stirred for another 4 hours. The solution was hydrothermally synthesized in a 4748 Type 125 mL PTFE-lined reactor (Parr Instrument Co.) and heated to 160 °C for 48 hours. The product was filtered and washed with water, ethanol, and acetone, then dried overnight at 60 °C. The precursor was heated to different temperatures and environments for 3 hours in order to form the different $LiVOPO_4$ polymorphs. Specifically, $\alpha_I$-$LiVOPO_4$ forms at 300 °C in Ar, β-$LiVOPO_4$ forms at 600 °C in $O_2$, and ε-$LiVOPO_4$ forms at 750 °C in Ar. Amorphized $LiVOPO_4{\cdot}2H_2O$ was prepared by subjecting the precursor to high-energy ball-milling for 30 minutes.

**Materials Characterization.** Powder X-ray diffraction (XRD) data was collected using a Bruker D8 Advance diffractometer utilizing a Cu $K\alpha$ source ($K\alpha1$ = 1.54053 Å, $K\alpha2$ = 1.54431 Å) over the 2θ range of 10 ° – 80 ° and a step size of 0.02 °. Indexing, phase identification, and Rietveld refinement were conducted using the TOPAS software package (Bruker AXS, version 5.0) and the PDF-2015 software package.

Thermogravimetric analysis coupled with mass spectrometry (TG-MS) was performed using a TG 209 F1 Iris coupled to a QMS 403 Aeolos Mass Spectrometer (260-TG/MS Netzsch).

In-situ diffraction data were collected using high-energy X-rays (λ = 0.2113 Å) provided by beamline 11-ID-B at the Advanced Photon Source, Argonne National Laboratory. Diffraction images were recorded in transmission geometry using an amorphous Si detector, and integrated with GSAS-II[40] using a $CeO_2$ standard (SRM674b) as calibrant. Powder samples were loaded in quartz capillaries and slightly compressed between two plugs of quartz wool. Capillaries were placed in the flow-cell/furnace[41] and $O_2$ or He was flown (4 cc/min) through the capillary during the heating. When He was flown through the cell, a residual gas analyzer (Pfeiffer PrismaPlus QMG 220 M2 mass spectrometer) was attached to the outlet to monitor released gases.

Transmission electron microscopy (TEM) was conducted by dispersing the as-synthesized β- or ε-$LiVOPO_4$ particles in ethanol, sonicating thoroughly, and then dropping the solution onto the carbon film coated copper grid. Microstructure characterization was performed on a Talos F200X S/TEM (Thermo fisher Scientific, USA) equipped with a field emission gun (FEG) operated at an accelerating voltage of 200 kV.

Samples for X-ray absorption spectroscopy (XAS) were prepared by thoroughly mixing ∼7 mg of $LiVOPO_4$ with ~70 mg of graphite and pressing into pellets of ~12 mm in diameter. Individual pellets were sealed between adhesive-coated Kapton tapes. Measurements were carried out in the transmission mode at the V K-edge of various $LiVOPO_4$ samples at the beamline 6BM of the National Synchrotron Light Source II (NSLS-II). The beamline is equipped with a Si(111) double crystal monochromator for which absolute energy calibration was carried out by measuring a reference foil of pure V simultaneously with the sample. An underfocused beam of 2.0 × 0.5 mm was used as a safeguard against possible beam damage. Higher harmonics were suppressed by the combination of harmonic rejection and focusing mirrors. The intensities of the incident beam ($I_0$) and the beam transmitted through the sample ($I_t$) and the reference foil ($I_{ref}$) were measured using gas-filled ionization chambers. All spectra were energy-calibrated with respect to the first peak in the derivative spectrum of the pure V reference foil. Data processing was carried out using the software ATHENA of the package IFEFFIT.[42] The normalized component of the EXAFS oscillation was transformed to $k$-space (i.e., wavenumber). The resultant $\chi(k)$ was multiplied by $k^3$ to emphasis the signal at high-k, Fourier transformed, and left uncorrected for a phase shift. In order to fit EXAFS data, a model spectrum was generated by performing *ab initio* calculations on respective structural models using the code FEFF8.2,[43] which was least-square fitted to the data using the software ARTEMIS of the package IFEFFIT. Details about EXAFS fitting procedure can be found elsewhere.[44, 45]

**Electrochemical Performance.** Electrochemical performance was evaluated by using $LiVOPO_4$ as the cathode material in 2325-type coin cells. The cathodes were prepared by first subjecting the $LiVOPO_4$ with graphene to high-energy ball-milling for 30 minutes. Polyvinyldiene fluoride (PVDF) was then added to the mixture, resulting in an $LiVOPO_4$:graphene:PVDF ratio of 75:15:10, and formed into a slurry using n-methyl-2-pyrrolidinone (NMP) as the solvent. The slurry was cast onto a carbon-coated Al foil and dried at 60 °C. Electrodes with areas of 1.2 $cm^2$ and active mass loadings of ~2.5 – 4.5 mg were punched and served as the cathodes. The cell was assembled with a pure lithium chip (MTI) as the counter and reference electrodes, a Celgard 2400 separator (Hoechst Celanese) as the separator, and 1 M $LiPF_6$ in 1:1 v/v ethylene carbonate (EC) and dimethyl carbonate (DMC) as the electrolyte. The cells were cycled at a rate of C/40 (C defined as 317 mAh/g) using a VMP multichannel potentiostat (Bio-Logic) from 1.5 V to 4.5 V at current densities from 16 – 28 μA/cm$^2$. Rate tests were conducted from C/100 up to C/2, then back to C/100, at 5 cycles each. Galvanostatic Intermittent Titration Technique (GITT) runs were conducted by discharging the cells at C/100 for 1.5 hours and letting them rest for 100 hours (high-voltage region) or 50 hours (low-voltage region).

### Computational Methods

All first-principles calculations in this work were performed using the Vienna *ab initio* simulation package (VASP) with the projected augmented wave (PAW) method. The Hubbard U extension to the Perdew-Burke-Ernzerhof (PBE) generalized gradient approximation (GGA) functional with a *U* value of 3.25 eV for vanadium was adopted.[46-48] All calculations were initialized in a ferromagnetic high spin configuration as previous studies have shown that magnetic effects have a minimal impact on relative energies.[29] A plane wave energy cutoff of 520 eV and k-point density of at least 1000/(number of atoms in the unit cell) were used for bulk relaxations of $\alpha_I$-, β-, and ε-$Li_xVOPO_4$ ($x$ = 0, 1). All other parameters are consistent with those used by the Materials Project for all calculations unless stated otherwise.[49] All data analysis was performed using the Python Materials Genomics (pymatgen) library.[50]

**Gibbs free energy.** Phonon calculations using density functional perturbation theory as implemented in the Phonopy code were carried out for $\alpha_I$-, β-, and ε-$Li_xVOPO_4$ (x = 0, 1).[51] The Gibbs free energy of each phase was then obtained based on the quasi-harmonic approximation. More stringent energy and force convergence criteria of $10^{-8}$ eV and $10^{-4}$ eV/Å respectively, were used for these calculations.

**Defect formation energy.** The defect formation energies ($E_d$) of O-vacancy and O-interstitial defects were calculated using the following equations:

O-vacancy: $E_d = E_{Li_{32}V_{32}P_{32}O_{159}} - E_{Li_{32}V_{32}P_{32}O_{160}} + \Delta\mu_O$

O-interstitial: $E_d = E_{Li_{32}V_{32}P_{32}O_{161}} - E_{Li_{32}V_{32}P_{32}O_{160}} - \Delta\mu_O$

where $\Delta\mu_O = \mu_O - \frac{1}{2}\mu_{O2}^0$ being the oxygen chemical potential relative to $\mu_{O2}^0$, the reference chemical potential of $O_2$ gas at standard temperatures and pressure. The defect concentration of 3.125% was simulated by creating (vacancy or interstitial) defects in a 2 × 2 × 2 supercell for β- and ε-$Li_xVOPO_4$ and 4 × 2 × 2 supercell for $\alpha_I$-$Li_xVOPO_4$ ($x$ = 0, 1). The structure was relaxed until the energy and forces are converged to $10^{-4}$ eV and 0.05 eV/Å, respectively.

**Surfaces.** Surface energies were calculated using the slab method, with the specific implementation and parameters as described by Tran et al.[52] All slabs investigated have symmetrically equivalent surfaces to avoid the creation of a dipole, i.e., they are of the Tasker Type II configuration[53]. For this portion of the work, we have focused our efforts on the more stable β and ε polymorphs for which we have detailed experimental data. We have not studied the less stable $\alpha_I$ polymorph as its bulk symmetry is low, making it difficult to construct Tasker II slab models. Similar to previous work on the $LiFePO_4$ cathode, only terminations that do no break P-O bonds were investigated.[53, 54] Only surfaces up to a max Miller index of 2 were considered, resulting in 29, 18, 19 and 19 facets for ε-$LiVOPO_4$, ε-$VOPO_4$, β-$LiVOPO_4$, and β-$VOPO_4$ respectively. We investigated non-polar, symmetric O adsorption on both surfaces of the slab using the algorithm implemented in pymatgen.[55] Only slabs corresponding to the facets appearing on the clean Wulff shapes of β- and ε-$LiVOPO_4$ were investigated. To calculate the surface energy, we used the surface grand potential:

$$\boldsymbol{\gamma = \frac{1}{2A}[E^{slab} - \sum_i N_i\mu_i]}$$

where $E^{slab}$ is the total energy of the slab with $i$ unique species, $\mu_i$ is the chemical potential of a species $i$ and $N_i$ is the total number of $i$ atoms in the slab. Further details are given in the SI for interested readers.

## Results

### Phase transformation upon heating oh $LiVOPO_4{\cdot}2H_2O$

Pure-phase $LiVOPO_4{\cdot}2H_2O$ (Figure S1) is used as a precursor to form the different polymorphs of $LiVOPO_4$. From thermogravimetric analysis (TGA), we observe that both temperature and atmosphere are key factors which cause different weight changes within the precursor (Figure S2). We can directly identify these specific changes using in-situ XRD while heating $LiVOPO_4{\cdot}2H_2O$ and use Rietveld refinement to quantify the relative amounts of each $LiVOPO_4$ polymorph at each specific temperature, as shown in Fig. 1. Two major observations can be made. Firstly, we observe that heating $LiVOPO_4{\cdot}2H_2O$ results in the formation of $\alpha_I$-$LiVOPO_4$, followed by β-$LiVOPO_4$, then ε-$LiVOPO_4$. This trend is seen in both Ar and $O_2$. Secondly, we observe that a large amount of β-$LiVOPO_4$ can only form in an oxidizing atmosphere.

Ex-situ XRD of heated $LiVOPO_4{\cdot}2H_2O$ (Figure S3) and Rietveld refinement of these spectra (Figure S4) also show similar trends, where $LiVOPO_4{\cdot}2H_2O \rightarrow \alpha_I$-$LiVOPO_4 \rightarrow$ β-$LiVOPO_4 \rightarrow$ ε-$LiVOPO_4$, and higher amounts of β-$LiVOPO_4$ only form when the samples are heated in an oxidizing atmosphere. In fact, heating $LiVOPO_4{\cdot}2H_2O$ at 600 °C in Ar, air, and $O_2$ results in 48%, 93%, and 97% β-$LiVOPO_4$, respectively, with the remainder being ε-$LiVOPO_4$.

Among the different ex-situ samples, the highest purity of $\alpha_I$-, β-, and ε-$LiVOPO_4$ were formed by heating $LiVOPO_4{\cdot}2H_2O$ to 300 °C in Ar, 600 °C in $O_2$, and 750 °C in Ar, respectively (Figure S5). XAS was then used to further show the purity of each phase. The pre-edge region of the V K-edge absorption spectra has shown remarkable sensitivity towards V valence in vanadyl phosphates,[11, 18, 45, 56] which can also be utilized in the present work. The main edge of the hydrated precursor $LiVOPO_4{\cdot}2H_2O$ and the sample heated to 300 °C in Ar (Figure S6) overlap with that of $\alpha_I$-$LiVOPO_4$, divulging little information on V valence. In contrast, the pre-edge region of these samples evolves

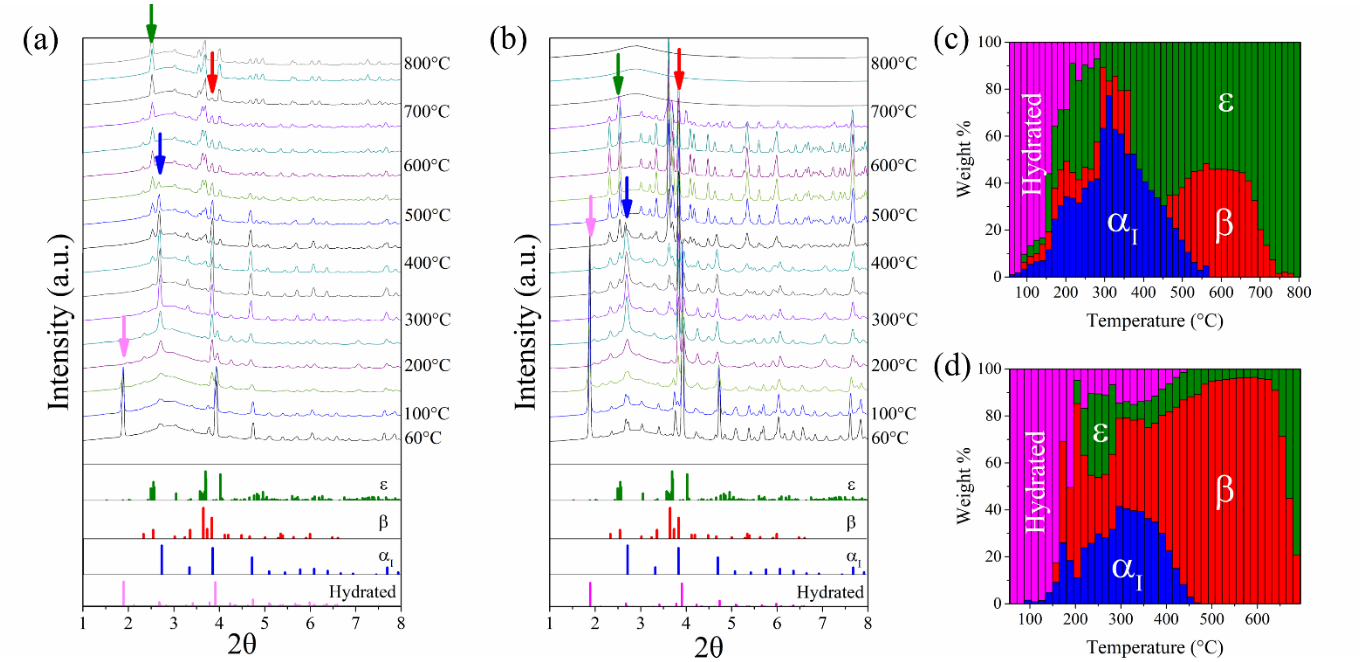

Fig. 1. In-situ XRD of $LiVOPO_4·2H_2O$ in (a) He and (b) $O_2$, with phase quantification of the different polymorphs from the XRD patterns in (c) He and (d) $O_2$.

differently in terms of pre-peak intensity. The reduced pre-peak intensity for hydrated sample is consistent with the lower oxidation state of V in $LiVOPO_4·2H_2O$ (i.e. $V^{3+}$)[45, 56] than in $\alpha_I$-$LiVOPO_4$ (i.e. $V^{4+}$). Interestingly, the sample heated to 300 °C also shows reduced pre-peak intensity, which is otherwise expected to fully evolve similar to that of $\alpha_I$-$LiVOPO_4$ upon removal of water and oxidation of $V^{3+}$ to $V^{4+}$ during heating. This $V^{3+}$ may likely be linked to the presence of unidentified impurity/metastable phase in the heated sample as detected by small impurities in the XRD.

A close structural resemblance between the orthorhombic $LiVOPO_4·2H_2O$[23] and tetragonal $\alpha_I$-$LiVOPO_4$[22] gives rise to similar local atomic arrangements as depicted by the EXAFS data (Figure S6), which were explained by the respective structural models (Figure S7). On the other hand, the samples heated to 600 °C in $O_2$ and 750 °C in Ar have their near-edge regions and EXAFS data evolve very similarly to those of the β-$LiVOPO_4$ and ε-$LiVOPO_4$ references, respectively. Fits to the EXAFS data of these samples based on the respective structural models (Figure S7) confirm transformations of hydrated $LiVOPO_4·2H_2O$ precursor to orthorhombic β-$LiVOPO_4$[26] and triclinic ε-$LiVOPO_4$[57] polymorphs upon heating to 600 °C and 750 °C, respectively. Although each phase can now be synthesized with high purity, the reasons behind the transformations between these phases are still not fully understood. Fig. 2 shows that the $LiVOPO_4·2H_2O$ to $\alpha_I$-$LiVOPO_4$ transformation can be attributed to fact that the $\alpha_I$- $LiVOPO_4$ structure is analogous to the $LiVOPO_4·2H_2O$ structure but without the water and with a slight shift in the Li position.[23]

$\alpha_I$-$LiVOPO_4$ can be heated to transform into both β- and ε-$LiVOPO_4$ (Figure S8 & Figure S9). However, it is observed that the reverse reaction, that is, the transformation of β- and ε-$LiVOPO_4$ into $\alpha_I$-$LiVOPO_4$, is not possible (Figure S10). In fact, when $\alpha_I$-$LiVOPO_4$ is kept at 300 °C in Ar (the conditions for the $LiVOPO_4·2H_2O$ → $\alpha_I$-$LiVOPO_4$ transformation) for extended periods, it slowly transforms into a mixture of β- and ε-$LiVOPO_4$.

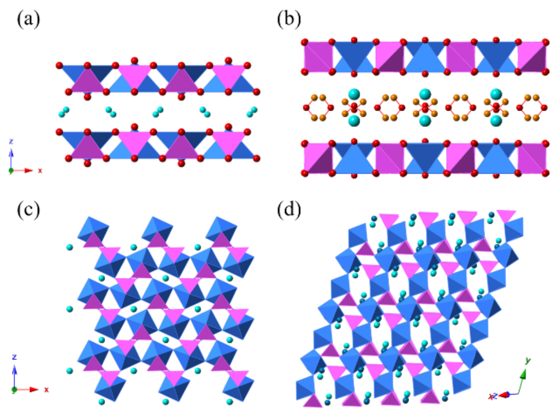

Fig. 2. Crystal structure of (a) $\alpha_I$-$LiVOPO_4$, (b) $LiVOPO_4·2H_2O$, (c) β-$LiVOPO_4$, and (d) ε-$LiVOPO_4$ showing the orientation of the PO tetrahedral (magenta), $VO_6$ octahedra (blue), Li (aqua) and water (red and yellow).

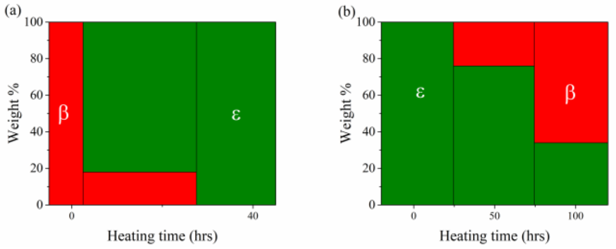

Fig. 3. Phase quantification of (a) β-$LiVOPO_4$ transformation to ε-$LiVOPO_4$ (750 °C, Ar) and (b) ε-$LiVOPO_4$ transformation to β-$LiVOPO_4$ (600 °C, $O_2$).

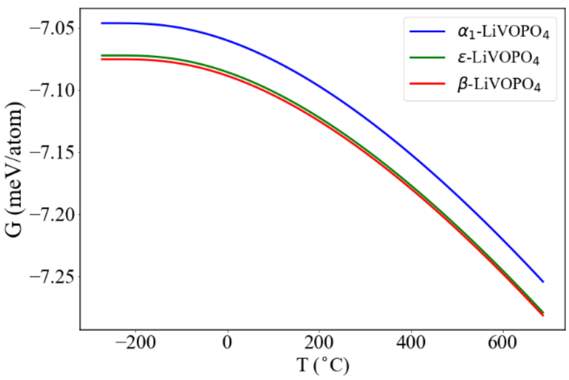

Fig. 4. Calculated Gibbs free energies (G) of $\alpha_I$-, β-, and ε-$LiVOPO_4$ as a function of temperature.

All these observations suggest that $\alpha_I$-$LiVOPO_4$ is metastable relative to β- and ε-$LiVOPO_4$.

Finally, we observe that β-$LiVOPO_4$ can transform into ε-$LiVOPO_4$ and vice versa. The phase distribution when β-$LiVOPO_4$ is heated for extended periods in Fig. 3a shows that β-$LiVOPO_4$ readily transforms into ε-$LiVOPO_4$ when heated at 750 °C in Ar. Similarly, Fig. 3b shows that ε-$LiVOPO_4$ also transforms into β-$LiVOPO_4$ when heated at 600 °C in $O_2$, albeit at a slower rate.

Fig. 4 presents the calculated Gibbs free energies of $\alpha_I$-, β-, and ε-$LiVOPO_4$ within the temperature range of 0 – 1000 K. We observe that the Gibbs free energies of ε-$LiVOPO_4$ and β-$LiVOPO_4$ are almost degenerate (within 3 meV/atom of each other) and much lower than that of $\alpha_I$-$LiVOPO_4$ at all temperatures of interest. This clearly indicates that the $\alpha_I$ phase is the most unstable phase, which is consistent with our experimental observations and previously reported calculations.[16, 29] Additionally, the small difference in energies between β- and ε-$LiVOPO_4$ explain why it is possible to reversibly transform between these phases.

### Role of Oxygen in the Phase Stability of the Different $LiVOPO_4$ Polymorphs

It is observed in both in-situ and ex-situ heating of $LiVOPO_4{\cdot}2H_2O$ that the presence of $O_2$ in the atmosphere during heating has a drastic effect on the relative ratios of β- and ε-$LiVOPO_4$. This effect of $O_2$ on stability can be more clearly demonstrated when heating amorphized $LiVOPO_4{\cdot}2H_2O$. Fig. 5 shows that, when heated to 600 °C, amorphized $LiVOPO_4{\cdot}2H_2O$ forms β-$LiVOPO_4$ in $O_2$ or ε-$LiVOPO_4$ in Ar. This result shows that, independent of temperature, the preferential formation of β- or ε-$LiVOPO_4$ is largely dictated by the presence of $O_2$ in the atmosphere.

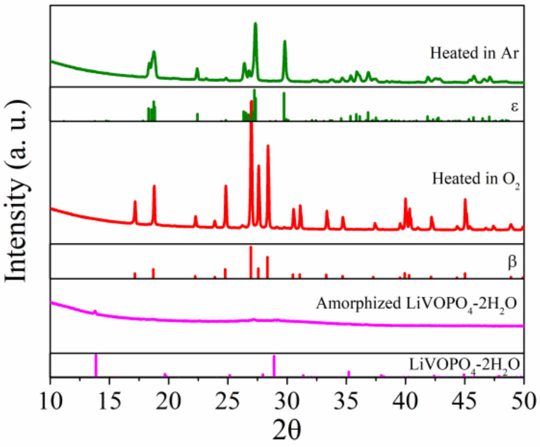

Fig. 5. XRD of amorphized $LiVOPO_4{\cdot}2H_2O$ before and after heating at 600 °C in different atmospheres.

In order to further understand the effect of $O_2$ on the stability of these phases, we monitored the release of $O_2$ gas during the β-to-ε-$LiVOPO_4$ transformation and how they match with changes in the XRD patterns, and weight. Fig. 6a shows, from in-situ XRD, that the onset of the β-to-ε transformation at around 630 °C matches well with the onset of $O_2$ release, as detected by the RGA. Additionally, the $O_2$ signal diminishes once the maximum amount of ε-$LiVOPO_4$ is formed. This alignment of the XRD and RGA data show that the formation of ε-$LiVOPO_4$ and the release of $O_2$ are related. Similarly, Fig. 6b shows that the loss of $O_2$ can be detected and quantified using a TG-MS. The maximum weight loss coincides with the maximum amount of detected $O_2$ loss, both at around 650 °C. This fits with the observations made from the β-to-ε in-situ XRD. Additionally, the thermogram shows that the amount of $O_2$ lost during heating is ~0.078% of the total weight, which is ~0.0065 moles of O per mole of $LiVOPO_4$.

Using TGA, it is also possible to observe the weight changes during the reverse transformation, from ε-$LiVOPO_4$ to β-

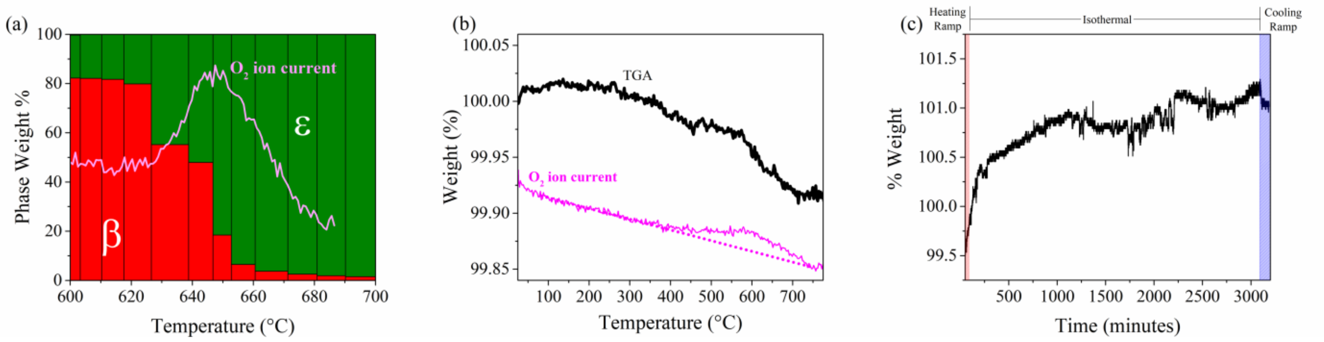

Fig. 6. Different changes during the β ↔ ε transformation: (a) phase quantification of in-situ XRD heating of β-$LiVOPO_4$ in He and RGA signal of $O_2$, (b) TG-MS of β-$LiVOPO_4$ heated in $N_2$, and (c) TGA of ε-$LiVOPO_4$ held at 580 °C in $O_2$.

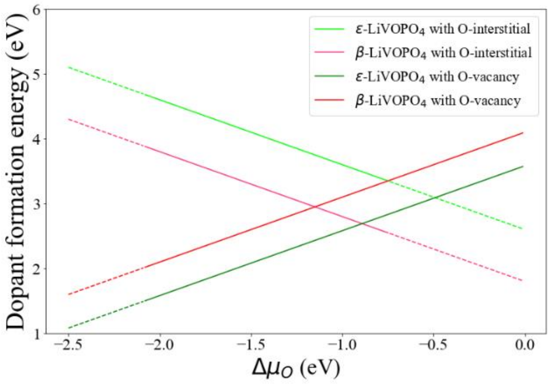

Fig. 7. Calculated defect formation energies of (a) O-vacancy and (b) O-interstitial for β- and ε-LiVOPO$_4$ with respect to $\Delta\mu_O$. To avoid decomposition of LiVOPO$_4$, $-2.08 < \Delta\mu_O < -0.74$ eV, as indicated by the dash lines.

LiVOPO$_4$. Fig. 6c shows that heating ε-LiVOPO$_4$ at 580°C for 50 hours in O$_2$ causes a weight gain of ~2%. XRD of the resultant product shows that we are able to convert 69% of ε-LiVOPO$_4$ into β-LiVOPO$_4$ (Figure S13). It is possible that when ε-LiVOPO$_4$ transforms into β-LiVOPO$_4$, it takes in O from the atmosphere, possibly to fill O-vacancies. Overall, Fig. 6 suggests that ε-LiVOPO$_4$ has more O-vacancies than β-LiVOPO$_4$, and that these vacancies affect the stability of both phases.

Fig. 7 presents the calculated defect formation energies of O-vacancies and interstitials in β- and ε-LiVOPO$_4$ relative to $\Delta\mu_O$. We find that at low oxygen chemical potentials (higher temperatures or reducing atmospheres), the most stable defect structure is that of ε-LiVOPO$_4$ with O-vacancies. Conversely, at high oxygen chemical potentials (lower temperatures or O$_2$ atmospheres), the most stable defect structure is that of β-LiVOPO$_4$ with O-interstitials.

The calculated dopant formation energies of O-vacancies in β-LiVOPO$_4$ are larger than that of ε-LiVOPO$_4$, while the energies of the O-interstitials of β-LiVOPO$_4$ are lower than that of ε-LiVOPO$_4$. These findings suggest that β-LiVOPO$_4$ is more likely to form in the presence of O-interstitials, and ε-LiVOPO$_4$ is preferred in the presence of O-vacancies. These calculation results are consistent with the experimental observations above.

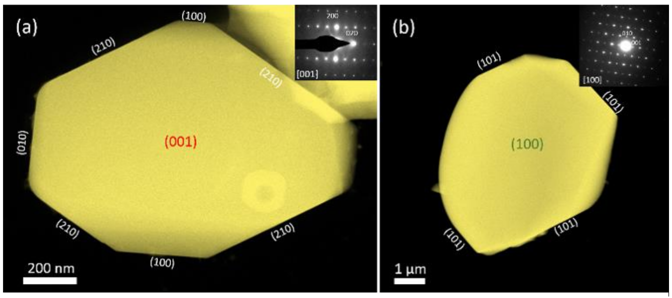

Fig. 9. TEM image of (a) β- and (b) ε-LiVOPO$_4$ showing the major facets.

## Surface stability of LiVOPO$_4$ polymorphs

For β- and ε-LiVOPO$_4$, all facets remain non-polar after structural relaxations. It is shown that LiO$_6$ and VO$_6$ octahedra are cut through, leading to undercoordinated Li and V atoms on the surface in each orientation. We used the coordination loss model developed by Wang et al.[53, 54] to determine the contributions of each $i$-fold Li and $j$-fold V to surface energy with $i$ and $j$ being the oxygen coordination number for Li and V respectively (see Table S2. Contributions of various coordinated V ($\mathrm{f_i}$) and Li ($\mathrm{l_j}$) to the surface energy.). For β-LiVOPO$_4$, we see a positive contribution to surface energy for both Li and V which increases with undercoordination. An exception to this is the negative contribution due to 4-fold Li. This is consistent with previous observations for LiFePO$_4$.[53, 54] For ε-LiVOPO$_4$, the positive energy contributions of $i$-fold V increases with undercoordination. However, we observe a significant negative contribution due to the 2-fold Li. The lowest-energy structures of each facet are provided in CIF format in the SI.

Fig. 8 plots the fractional areas of the different facets on the Wulff shape against $\Delta\mu_O$ for β- and ε-LiVOPO$_4$ along with insets of the Wulff shapes constructed based on calculated surface energies (Figure S14). For a max Miller index of 2, there are 19 and 29 symmetrically distinct facets for the clean β- and ε-LiVOPO$_4$, respectively. However, only 11 and 12 of these facets are thermodynamically stable on the Wulff shapes of clean β- and ε-LiVOPO$_4$, respectively. The calculated surface energies for most facets of β-LiVOPO$_4$ are higher than those reported

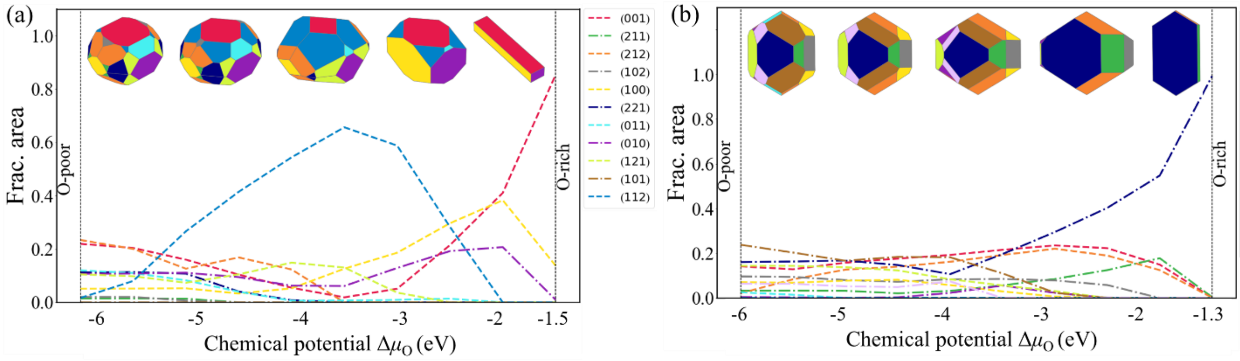

Fig. 8. The fractional area of different facets and the Wulff shape as a function of $\Delta\mu_O$ for (a) β- and (b) ε-LiVOPO$_4$.

Table 1. Calculated redox potentials for the extraction of Li from different surfaces on the Wulff shape of $LiVOPO_4$, with the bulk potential provided for comparison.

| | | | | | | | | | | | | | | |
|---|---|---|---|---|---|---|---|---|---|---|---|---|---|---|
| β-$LiVOPO_4$ | Facet | (121) | (221) | (011) | (211) | (102) | (001) | (212) | (112) | (010) | (100) | (101) | | Bulk |
| | Voltage (V) | 4.51 | 4.35 | 4.33 | 4.12 | 4.02 | 3.88 | 3.83 | 3.75 | 3.71 | 3.18 | 3.03 | | 3.83 |
| ε-$LiVOPO_4$ | Facet | (111) | (201) | (100) | (102) | $(1\bar{1}2)$ | $(1\bar{2}0)$ | (120) | (012) | $(1\bar{2}2)$ | $(2\bar{1}2)$ | (211) | $(1\bar{1}0)$ | Bulk |
| | Voltage (V) | 4.63 | 4.17 | 3.82 | 3.79 | 3.63 | 3.45 | 3.36 | 3.28 | 3.15 | 3.14 | 3.12 | 3.12 | 3.80 |

recently by Li *et al.*[38], and we attribute these differences to slightly different parameter settings. One exception is the (101) facet of β-$LiVOPO_4$, which we calculate to be 0.98 $J/m^2$, (0.42 $J/m^2$ lower than the value reported by Li *et al*.). We also find that the (121), (102), (212), (211), (221), and (112) facets, which were not considered by Li et al., contribute to the Wulff shape of clean β-$LiVOPO_4$ as well.

The Wulff shape of β-$LiVOPO_4$ becomes more anisotropic as $\Delta\mu_O$ increases, finally forming a rectangular rod under extreme oxidizing conditions enclosed by the (001), (100), and (010) planes. A similar behavior in the evolution of the Wulff shape for ε-$LiVOPO_4$ is observed as the fractional area of the (100) facet sharply increases as $\Delta\mu_O$ increases beyond -3 eV.

In Fig. 9, TEM images of the particles of β- and ε-$LiVOPO_4$ show that the β-$LiVOPO_4$ is enclosed at the top by the (001) plane and to the sides with the (010) and (100) planes while ε-$LiVOPO_4$ is enclosed at the top by the (100) plane, both of which are in excellent agreement with the dominant facets on the calculated Wulff shapes. However, the (210) facet which is present in the experimental particle morphology shown in Fig. 9a is not present in the Wulff shape evolution of β-$LiVOPO_4$.

### Surface redox potentials

Table 1 shows the calculated redox potentials to extract Li from different facets on the Wulff shape of $LiVOPO_4$. The surface potentials vary from 4.51 to 3.03 V and 4.63 to 3.12 V for β-$LiVOPO_4$ and ε-$LiVOPO_4$ respectively. The calculated bulk redox potentials for β-$LiVOPO_4$ and ε-$LiVOPO_4$ are 3.83 V and 3.80 V, respectively, which are in good agreement with the experimental voltage of ~4.0 V.[21, 31, 58]

### Comparison of electrochemical performance of different $LiVOPO_4$ polymorphs

Fig. 10a shows the charge-discharge curve of the first cycle of each of the $LiVOPO_4$ polymorphs. We can observe that β-$LiVOPO_4$ has the highest capacity among the different phases, which may be attributed to its better kinetics,[16] and the higher rate capability on the surfaces of β-$LiVOPO_4$ as seen in the longer high-voltage plateau. Fig. 10b shows that this larger capacity is maintained over several cycles. Fig. 10c and Fig. 10d show that the experimental voltage of each plateau for both the high- and low-voltage regions fit well with theoretical voltage calculations which we reported previously.[16]

The high-voltage rate capability test in Fig. 10e shows that all three phases experience the expected capacity loss as they are cycled at higher rates, and regain this lost capacity when cycled at lower rates. This is in agreement with the GITT data in Fig. 10g, which shows that each phase experiences comparable voltage changes when reaching equilibrium upon rest. A similar analysis can be conducted in the low-voltage region, shown in Fig. 10f. First, we observe that $\alpha_I$-$LiVOPO_4$ experiences a similar loss in capacity when cycled at higher rates. Interestingly, β- and ε-$LiVOPO_4$ show barely any loss of capacity when cycled at higher rates in the low-voltage region. This is also observed in the GITT in Fig. 10h, where both β- and ε-$LiVOPO_4$ only experience a small overpotential, while $\alpha_I$-$LiVOPO_4$ experiences

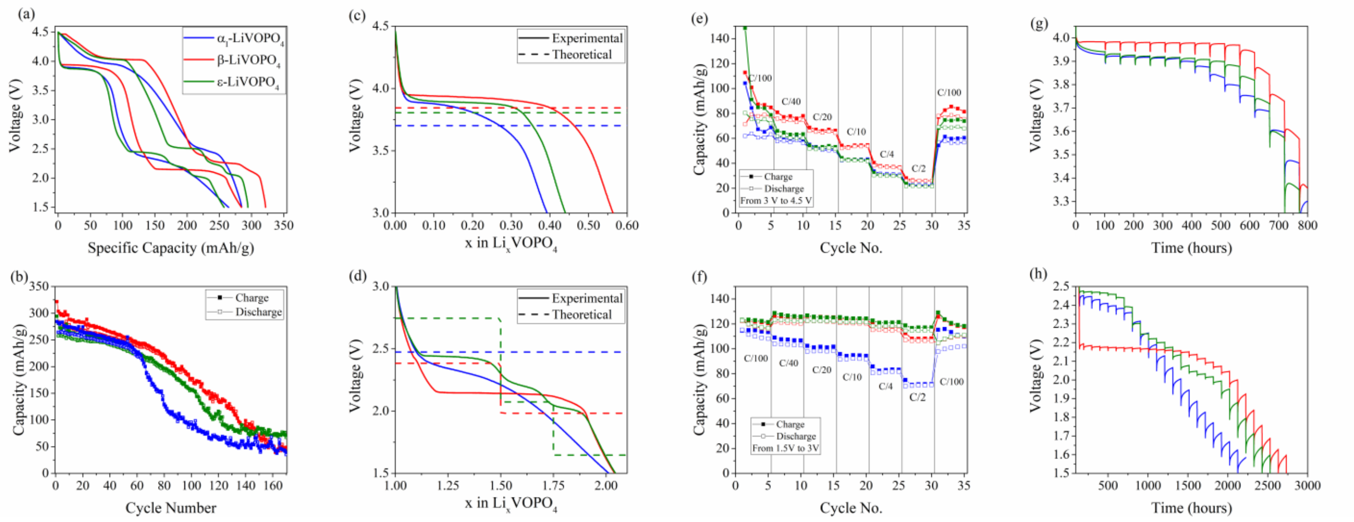

Fig. 10. Comparison of electrochemical performance of different $LiVOPO_4$ polymorphs: (a) first discharge-charge capacity; (b) capacity retention over several cycles; theoretical vs experimental voltage plateaus in the (c) high- and (d) low-voltage regions; rate tests in the (e) high- and (f) low-voltage regions; GITT in the (g) high- and (h) low-voltage regions.

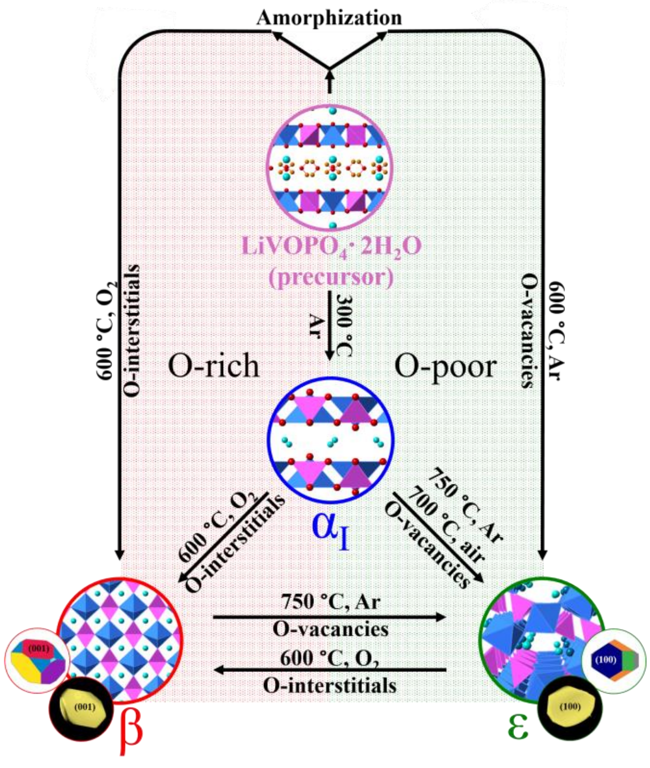

Fig. 11. Summary of different LiVOPO$_4$ transformation conditions and products.

a large change in voltage. This indicates that both β- and ε-LiVOPO$_4$ have better kinetics in this low-voltage regime. We also observe for all polymorphs that the low-voltage region nearly reaches the full theoretical capacity, while the high-voltage region is still lacking in capacity.

## Discussion

In our previous study[16], we showed that, in regard to thermodynamic stability, $\alpha_I$-LiVOPO$_4$ <<< ε-LiVOPO$_4$ ≤ β-LiVOPO$_4$ at 0 K. In this study, we found the phase stability from 0 – 1000 K exhibits the same trend for the three phases via calculating Gibbs free energies. In particular, β- and ε- LiVOPO$_4$ show little difference in Gibbs free energy, which explains why there is a small amount of ε-LiVOPO$_4$ always involved when synthesizing β-LiVOPO$_4$ at low temperatures in either O$_2$ or Ar atmospheres. Additionally, the energetics suggests that it is possible to reversibly transform between these two phases. We can observe this transformation by taking ex-situ XRD of β-LiVOPO$_4$ heated in the conditions used to synthesize ε-LiVOPO$_4$ and vice versa (Figure S11).

We have also clearly shown that O$_2$ plays an important role in the formation of β-LiVOPO$_4$ over ε-LiVOPO$_4$. The lower O-interstitial formation energy in β-LiVOPO$_4$ indicates that it forms more favorably in O-rich environments. In contrast, ε-LiVOPO$_4$ is the preferred phase in O-deficient environments due to its lower O-vacancy formation energy. Consequently, at high temperatures above 750 ℃ in Ar, we can achieve pure ε-LiVOPO$_4$. In addition, we found that the rate of transformation from β-LiVOPO$_4$ into ε-LiVOPO$_4$ at 750 °C is much faster than that of the reverse process at 600 °C. This is likely because the transformation from β-LiVOPO$_4$ into ε-LiVOPO$_4$ via O$_2$ release at high temperatures is kinetically more favorable than the reverse reaction via O$_2$ incorporation at low temperatures.

For β-LiVOPO$_4$, we found that (001), (100), and (010) are the dominant facets on the Wulff shape under oxidizing conditions, which are confirmed via TEM. Under extremely oxidizing conditions, we find that rectangular rods may be formed due to the fact that the (001) and (100) facets have a relatively higher coverage of oxygen (as shown by their steeper slopes in Figure S14.) than other facets, which results in a lower surface energy than other facets. In addition, we found that the (100) and (010) facets have redox potentials of 3.18 V and 3.71 V, respectively, lower than the 3.83 V of the bulk, in agreement with the results reported by Li *et al.*[38] The lower surface redox potentials can lead to easier Li-ion extraction and hence increasing the surface area of these two facets in oxidizing environments would facilitate the rate capability of β-LiVOPO$_4$ on the surface. In contrast, the dominant facet of ε-LiVOPO$_4$ is (100) under the extreme oxidizing condition, which has a redox potential of 3.82 V, higher than 3.80 V of bulk. This indicates oxidizing atmosphere is likely with little effect on improving the performance of ε-LiVOPO$_4$. The improved rate capability of β-LiVOPO$_4$ on the surface along with its better ionic kinetics[16] may explain why it achieves the best electrochemical performance among the three phases studied.

An overall summary of all the results presented here is shown in Fig. 11.

## Conclusion

In summary, we conducted a thorough study on the effects of temperature and environment on the stability and formation of the different polymorphs of LiVOPO$_4$ using a single precursor, LiVOPO$_4$·2H$_2$O. Heating the precursor resulted in the following transformation: $\alpha_I$-LiVOPO$_4$ → β-LiVOPO$_4$ ↔ ε-LiVOPO$_4$. The phase stability from 0 – 1000 K via Gibbs free energy calculations for the three phases is: $\alpha_I$-LiVOPO$_4$ <<< ε-LiVOPO$_4$ ≤ β-LiVOPO$_4$, which is consistent with the experimental phase transformation process. The higher O-interstitial and lower O-vacancy defect formation energies of β-LiVOPO$_4$ and ε-LiVOPO$_4$, respectively, indicate that β-LiVOPO$_4$ and ε-LiVOPO$_4$ preferentially form in O-rich and O-deficient environments, respectively. Consequently, we can achieve the largest amount of β-LiVOPO$_4$ phase in oxidizing atmospheres and pure ε-LiVOPO$_4$ phase in Ar atmospheres at high temperatures (> 750 °C). The evolution of Wulff shapes with O chemical potentials indicates that only the surface rate performance of β-LiVOPO$_4$ can be improved by synthesis under O-rich environments. The calculated dominant facets of β-, and ε-LiVOPO$_4$ are further verified on the experimental particle morphologies by TEM. Finally, extensive electrochemical testing shows that of the three LiVOPO$_4$ phases, the β phase is the most promising cathode material with the highest capacity and best rate capability. This may be attributed to its superior ionic kinetics and rate performances on the surfaces as the particle size approaches the nanoscale.

## Conflicts of interest

There are no conflicts to declare

## Acknowledgements

This work was supported by the NorthEast Center for Chemical Energy Storage (NECCES), an Energy Frontier Research Center funded by the U.S. Department of Energy, Office of Science, Office of Basic Energy Sciences under Award Number DE-SC0012583. It used resources of the Advanced Photon Source, a U.S. Department of Energy (DOE) Office of Science User Facility operated for the DOE Office of Science by Argonne National Laboratory under Contract No. DE-AC02-06CH11357. We acknowledge computational resources provided by the Triton Shared Computing Cluster (TSCC) at the University of California, San Diego, the National Energy Research Scientific Computing Center (NERSC), and the Extreme Science and Engineering Discovery Environment (XSEDE) supported by the National Science Foundation under Grant No. ACI-1053575. Y.-C. Lin, R. Tran, I-H Chu, Z. Wang, X. Li and S. P. Ong also acknowledge data and software resources provided by the Materials Project, funded by the U.S. Department of Energy, Office of Science, Office of Basic Energy Sciences, Materials Sciences and Engineering Division under Contract No. DE-AC02-05-CH11231: Materials Project program KC23MP.

## References

1. M. S. Whittingham, *Proceedings of the IEEE*, 2012, **100**, 1518-1534.
2. L. Lu, X. Han, L. Jianqiu, J. Hua and M. Ouyang, *A review on the key issues for lithium-ion battery management in electric vehicles*, 2013.
3. M. S. Whittingham, *Chemical Reviews*, 2014, **114**, 11414-11443.
4. G. E. Blomgren, *Journal of The Electrochemical Society*, 2017, **164**, A5019-A5025.
5. M. S. Whittingham, *Chemical Reviews*, 2004, **104**, 4271-4302.
6. V. Etacheri, R. Marom, R. Elazari, G. Salitra and D. Aurbach, *Challenges in the Development of Advanced Li-Ion Batteries: A Review*, 2011.
7. C. Renjie, L. Rui, H. Yongxin, W. Feng and L. Li, *Advanced Science*, 2016, **3**, 1600051.
8. G. Hautier, A. Jain, T. Mueller, C. Moore, S. P. Ong and G. Ceder, *Chemistry of Materials*, 2013, **25**, 2064-2074.
9. C. Wang, M. Sawicki, S. Emani, C. Liu and L. L. Shaw, *Electrochimica Acta*, 2015, **161**, 322-328.
10. J. Liu, L. Yin, X.-Q. Yang and P. G. Khalifah, *Chemistry of Materials*, 2018, **30**, 4609-4616.
11. J. Ding, Y.-C. Lin, J. Liu, J. Rana, H. Zhang, H. Zhou, I.-H. Chu, K. M. Wiaderek, F. Omenya, N. A. Chernova, K. W. Chapman, L. F. J. Piper, S.-P. Ong and M. S. Whittingham, *Advanced Energy Materials*, 2018, **8**, 1800221.
12. M. Armand and J. M. Tarascon, *Nature*, 2008, **451**, 652.
13. X.-P. Gao and H.-X. Yang, *Energy & Environmental Science*, 2010, **3**, 174-189.
14. K. Sung-Wook, S. Dong-Hwa, M. Xiaohua, C. Gerbrand and K. Kisuk, *Advanced Energy Materials*, 2012, **2**, 710-721.
15. G. Hautier, A. Jain, S. P. Ong, B. Kang, C. Moore, R. Doe and G. Ceder, *Chemistry of Materials*, 2011, **23**, 3495-3508.
16. Y.-C. Lin, M. F. V. Hidalgo, I.-H. Chu, N. A. Chernova, M. S. Whittingham and S. P. Ong, *Journal of Materials Chemistry A*, 2017, DOI: 10.1039/C7TA04558A.
17. Y.-C. Lin, B. Wen, K. M. Wiaderek, S. Sallis, H. Liu, S. H. Lapidus, O. J. Borkiewicz, N. F. Quackenbush, N. A. Chernova, K. Karki, F. Omenya, P. J. Chupas, L. F. J. Piper, M. S. Whittingham, K. W. Chapman and S. P. Ong, *Chemistry of Materials*, 2016, **28**, 1794-1805.
18. C. Siu, I. D. Seymour, S. Britto, H. Zhang, J. Rana, J. Feng, F. O. Omenya, H. Zhou, N. A. Chernova, G. Zhou, C. P. Grey, L. F. J. Piper and M. S. Whittingham, *Chemical Communications*, 2018, **54**, 7802-7805.
19. M. Bianchini, J. M. Ateba-Mba, P. Dagault, E. Bogdan, D. Carlier, E. Suard, C. Masquelier and L. Croguennec, *Journal of Materials Chemistry A*, 2014, **2**, 10182-10192.
20. K. L. Harrison, C. A. Bridges, C. U. Segre, C. D. Varnado, D. Applestone, C. W. Bielawski, M. P. Paranthaman and A. Manthiram, *Chemistry of Materials*, 2014, **26**, 3849-3861.
21. G. He, C. A. Bridges and A. Manthiram, *Chemistry of Materials*, 2015, **27**, 6699-6707.
22. N. Dupré, G. Wallez, J. Gaubicher and M. Quarton, *Journal of Solid State Chemistry*, 2004, **177**, 2896-2902.
23. S. A. Hameed, M. Nagarathinam, M. V. Reddy, B. V. R. Chowdari and J. J. Vittal, *Journal of Materials Chemistry*, 2012, **22**, 7206-7213.
24. M. Tachez, F. Theobald and E. Bordes, *Journal of Solid State Chemistry*, 1981, **40**, 280-283.
25. M. M. Ren, Z. Zhou, L. W. Su and X. P. Gao, *Journal of Power Sources*, 2009, **189**, 786-789.
26. K. H. Lii, C. H. Li, C. Y. Cheng and S. L. Wang, *Journal of Solid State Chemistry*, 1991, **95**, 352-359.
27. R. Gopal and C. Calvo, *Journal of Solid State Chemistry*, 1972, **5**, 432-435.
28. J.-M. Ateba Mba, C. Masquelier, E. Suard and L. Croguennec, *Chemistry of Materials*, 2012, **24**, 1223-1234.
29. C. Ling, R. Zhang and F. Mizuno, *Journal of Materials Chemistry A*, 2014, **2**, 12330-12339.
30. Y. Song, P. Y. Zavalij and M. S. Whittingham, *Journal of The Electrochemical Society*, 2005, **152**, A721-A728.
31. J. Barker, M. Y. Saidi and J. L. Swoyer, *Journal of The Electrochemical Society*, 2004, **151**, A796-A800.
32. Z. Liu, Z. Su and H. Tian, *International Journal of Electrochemical Science*, 2017, **12**, 10107 – 10114.
33. A. P. Tang, Z. Q. He, J. Shen and G. R. Xu, *Advanced Materials Research*, 2012, **554-556**, 436-439.
34. H. Zhou, Y. Shi, F. Xin, F. Omenya and M. S. Whittingham, *ACS Applied Materials & Interfaces*, 2017, DOI: 10.1021/acsami.7b07895.
35. N. Kenta, H. Tsuyoshi and K. Takayuki, *Journal of the American Ceramic Society*, 2008, **91**, 3920-3925.
36. L. Wang, L. Yang, L. Gong, X. Jiang, K. Yuan and Z. Hu, *Electrochimica Acta*, 2011, **56**, 6906-6911.

37. A. Van der Ven and G. Ceder, *Electrochemical and Solid-State Letters*, 2000, **3**, 301-304.

38. Y. Li, J. Zhang, F. Yang, J. Liang, H. Sun, S. Tang and R. Wang, *Physical Chemistry Chemical Physics*, 2014, **16**, 24604-24609.

39. L. Wang, F. Zhou, Y. S. Meng and G. Ceder, *Physical Review B*, 2007, **76**, 165435.

40. B. H. Toby and R. B. Von Dreele, *Journal of Applied Crystallography*, 2013, **46**, 544-549.

41. P. J. Chupas, K. W. Chapman, C. Kurtz, J. C. Hanson, P. L. Lee and C. P. Grey, *Journal of Applied Crystallography*, 2008, **41**, 822-824.

42. B. Ravel and M. Newville, *Journal of Synchrotron Radiation*, 2005, **12**, 537-541.

43. A. L. Ankudinov, B. Ravel, J. J. Rehr and S. D. Conradson, *Physical Review B*, 1998, **58**, 7565-7576.

44. J. Rana, M. Stan, R. Kloepsch, J. Li, G. Schumacher, E. Welter, I. Zizak, J. Banhart and M. Winter, *Advanced Energy Materials*, 2014, **4**, 1300998.

45. J. Rana, Y. Shi, M. J. Zuba, K. M. Wiaderek, J. Feng, H. Zhou, J. Ding, T. Wu, G. Cibin, M. Balasubramanian, F. Omenya, N. A. Chernova, K. W. Chapman, M. S. Whittingham and L. F. J. Piper, *Journal of Materials Chemistry A*, 2018, DOI: 10.1039/C8TA06469E.

46. A. I. Liechtenstein, V. I. Anisimov and J. Zaanen, *Physical Review B*, 1995, **52**, R5467-R5470.

47. S. L. Dudarev, G. A. Botton, S. Y. Savrasov, C. J. Humphreys and A. P. Sutton, *Physical Review B*, 1998, **57**, 1505-1509.

48. A. K. Padhi, K. S. Nanjundaswamy and J. B. Goodenough, *Journal of The Electrochemical Society*, 1997, **144**, 1188-1194.

49. A. Jain, S. P. Ong, G. Hautier, W. Chen, W. D. Richards, S. Dacek, S. Cholia, D. Gunter, D. Skinner, G. Ceder and K. A. Persson, *APL Materials*, 2013, **1**, 011002.

50. S. P. Ong, W. D. Richards, A. Jain, G. Hautier, M. Kocher, S. Cholia, D. Gunter, V. L. Chevrier, K. A. Persson and G. Ceder, *Computational Materials Science*, 2013, **68**, 314-319.

51. A. Togo and I. Tanaka, *Scripta Materialia*, 2015, **108**, 1-5.

52. R. Tran, Z. Xu, B. Radhakrishnan, D. Winston, W. Sun, K. A. Persson and S. P. Ong, *Scientific Data*, 2016, **3**, 160080.

53. P. W. Tasker, *Journal of Physics C: Solid State Physics*, 1979, **12**, 4977.

54. L. Wang, F. Zhou, Y. S. Meng and G. Ceder, *Physical Review B*, 2007, **76**, 165435.

55. J. H. Montoya and K. A. Persson, *npj Computational Materials*, 2017, **3**, 14.

56. Y. Shi, H. Zhou, I. D. Seymour, S. Britto, J. Rana, L. W. Wangoh, Y. Huang, Q. Yin, P. J. Reeves, M. Zuba, Y. Chung, F. Omenya, N. A. Chernova, G. Zhou, L. F. J. Piper, C. P. Grey and M. S. Whittingham, *ACS Omega*, 2018, **3**, 7310-7323.

57. A. V. Lavrov, V. P. Nikolaev, G. G. Sadikov and M. A. Poraj-Koshits, *Doklady Akademii Nauk SSSR*, 1982, **266**, 343-346.

58. B. M. Azmi, T. Ishihara, H. Nishiguchi and Y. Takita, *Journal of Power Sources*, 2003, **119-121**, 273-277.

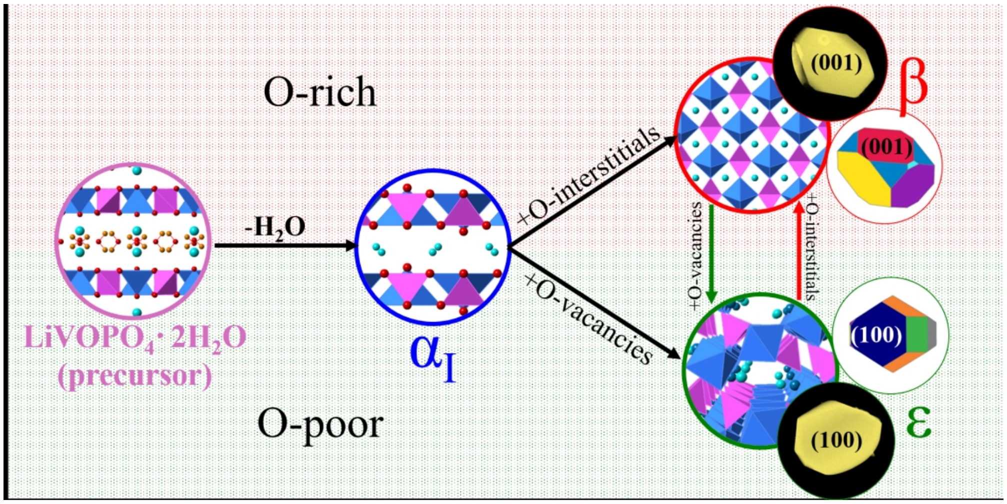

Abstract Figure

354x175mm (150 x 150 DPI)